Steps in gas-surface reactions

Lent, R. van

IGOR Pro procedures

This appendix contains IGOR Pro procedures that were used to simulate and/or analyze experimental data.

Beam profile simulation: orifice

The following procedure calculates the fractional overlap between two circles as a function of on-axis translation. The center of the two circles lie on this common axis. It is used in the beam profile experiments in chapter 2. It generates the solid lines in figure 2.7.

```
function circlecircle_intersection (r1, r2, d0, dmax, deltad)
 Variable r1, r2, d0, dmax, deltad
 Make /O /N=(abs((d0 - dmax) / deltad)+2) Overlap, d
 variable i
 deltad = (d0 - dmax) / (numpnts(Overlap)-1)
 for (i=0; i < numpnts(Overlap); i+=1)
  d[i] = d0 - i*deltad
  if (abs(d[i]) <= abs(r1-r2) && r1 >= r2)
   Overlap[i] = pi*r2^2
  elseif (abs(d[i]) <= abs(r1-r2) && r1 < r2)
   Overlap[i] = pi*r1^2
  else
   Overlap[i] = r1^2*acos((d[i]^2+r1^2-r2^2)/(2*abs(d[i])*r1)) +
                r2^2*acos((d[i]^2+r2^2-r1^2)/(2*abs(d[i])*r2)) -
                0.5*sqrt( (-abs(d[i])+r1+r2)*(abs(d[i])+r1-r2) *
                (abs(d[i])-r1+r2) * (abs(d[i])+r1+r2) )
```

```
  endif
 endfor
 wavestats /q Overlap
 Overlap = Overlap / v_max
End
```

Beam profile simulation: slit (vertical translation)

The following IGOR Pro procedure calculates the overlap between a rectangle and a circle as a function of on-axis translation. The centers of the circle and the rectangle lie on this common axis. The rectangle is wider than the circle diameter. It is used in the beam profile experiments in chapter 2. It generates the solid black line (vertical translation) in figure 2.8.

```
function circlerectangle_intersection (r1, x2, y2, d0, dmax, deltad)
 Variable r1, x2, y2, d0, dmax, deltad
 Make /O /N=(abs((d0 - dmax) / deltad)+2) Overlap, d
 variable i
 deltad = (d0 - dmax) / (numpnts(Overlap)-1)
 for (i=0; i < numpnts(Overlap); i+=1)
  d[i] = d0 - i*deltad
  if ( abs(d[i]) >= (r1 + 0.5*y2) )
   //no overlap
   Overlap[i] =  0
  elseif ( y2 > 2*r1 && abs(d[i]) < abs(0.5*y2-r1) )
   //rectangle is longer and wider than circle diameter (complete overlap)
   Overlap[i] =  pi*r1^2
  elseif ( abs(d[i]) > (r1 - 0.5*y2) )
   //Rectangle falls off the circle edge
   Overlap[i] =  r1^2 * acos( (abs(d[i]) - 0.5*y2) / r1) -
                 (abs(d[i])-0.5*y2)*sqrt( r1^2 - (abs(d[i])-0.5*y2)^2)
  else
   //The circle extends past the rectangle on both sides.
   Overlap[i] =  ( r1^2 * acos( (abs(d[i]) - 0.5*y2) / r1) -
                 (abs(d[i])-0.5*y2)*sqrt( r1^2 - (abs(d[i])-0.5*y2)^2) ) -
                 (r1^2 * acos( (abs(d[i]) + 0.5*y2) / r1) -
                 (abs(d[i]) + 0.5*y2)*sqrt( r1^2 - (abs(d[i]) + 0.5*y2)^2) )
  endif
 endfor
```

```
 Overlap = Overlap / (pi*r1^2)
End
```

Beam profile simulation: orifice (horizontal translation)

The following IGOR Pro procedure calculates the overlap between a rectangle and a circle as a function of on-axis translation. The centers of the circle and the rectangle lie on this common axis. The rectangle is narrower than the circle diameter. It is used in the beam profile experiments in chapter 2. It generates the solid red line (horizontal translation) in figure 2.8.

```
function circlerectang_leintersection2 (r1, x2, y2, d0, dmax, deltad)
 Variable r1, x2, y2, d0, dmax, deltad
 Make /O /N=(abs((d0 - dmax) / deltad)+2) Overlap, d
 variable i
 deltad = (d0 - dmax) / (numpnts(Overlap)-1)
 for (i=0; i < numpnts(Overlap); i+=1)
  d[i] = d0 - i*deltad
  if ( abs(d[i]) >= (r1 + 0.5*x2) )
   //rectangle is not crossing the circle
   Overlap[i] = 0
   Overlap[i] = r1^2 * asin(0.5*y2/r1) - 0.5*y2*sqrt(r1^2 - (0.5*y2)^2) +
   y2 * (sqrt(r1^2-(0.5*y2)^2) - (abs(d[i]) - 0.5*x2))
  elseif ( abs(d[i]) < (r1 + 0.5*x2) &&
           0.5*y2 < sqrt(r1^2 - (abs(d[i]) - 0.5*x2)^2) &&
           -sqrt (r1^2 - (0.5 * y2)^2) > (abs(d[i] - 0.5*x2)) > - r1 )
   Overlap[i] =  pi * r1^2 - 2 * ( r1^2*acos(0.5*y2/r1) -
                 0.5*y2*sqrt(r1^2 - (0.5*y2)^2)) -
                 (r1^2 * acos( (abs(d[i]) - 0.5*x2) /r1) -
                 (abs(d[i]) - 0.5*x2)*(sqrt( r1^2 - (abs(d[i])-0.5*x2)^2)))
  else
   Overlap[i] =  pi * r1^2 - 2 * ( r1^2*acos(0.5*y2/r1) -
                 0.5*y2*sqrt(r1^2 - (0.5*y2)^2))
  endif
 endfor
 Overlap = Overlap / (pi*r1^2)
```

End

Chopper gating function simulation

The following IGOR Pro procedure generates the IGOR Pro fit function used for Time of Flight analysis. The slit in the chopper blade generates a pulse of molecules. The length of this pulse broadens the peaks in the time of flight. We account for this broadening effect by broadening the fit function with the chopper gating function. The following IGOR Pro procedure uses a similar approach as vertical translation for the slit-shaped orifice. However, it calculates the gating function with the same temporal resolution as the time of flight data.

```
function chopper (freq)
 //chopper frequency
 variable freq
 variable r1, Y2, d0, dmax, deltad, r_chopper, i, dap
 // beam radius at chopper
 r1 = 0.23
 // slit width
 Y2 = 0.85
 //travel distance of chopper runs from d0 - > dmax
 d0 = -(0.23*2 + 0.85)/2
 // travel distance of chopper runs from d0 - > dmax
 dmax = (0.23*2 + 0.85)/2
 // chopper radius (to where it chops the molecular beam)
 r_chopper = 55.992
 // datapoint time constant
 dap = 5*10^-7
 deltad = 2*pi*dap * r_chopper * freq //
 make /O /N=(round(abs((d0-dmax) / deltad))+3) gating
 make /O /N=(round(abs((d0-dmax) / deltad))+3) timing
 make /O /N=(round(abs((d0-dmax) / deltad))+3) d
 dmax = (round(abs((d0-dmax)/deltad))+2)*2*pi*dap*r_chopper*freq/2
 d0 = -dmax
 deltad = (d0 - dmax) / (numpnts(d)-1)
```

```
string/G TMBstr = "TMB="
for (i=0; i < numpnts(d); i+=1)
 d[i] = d0 + i*2*pi*dap * r_chopper * freq
 if ( abs(d[i]) >= (r1 + 0.5*y2) )
  //No overlap
  gating[i] = 0
 elseif ( y2 > 2*r1 && abs(d[i]) < abs(0.5*y2-r1) )
  //circle is smaller than rectangle and completely overlaps
  gating[i] = pi*r1^2
 elseif ( abs(d[i]) > (r1 - 0.5*y2) )
  //Rectangle is narrower than circle and only partially overlaps circle
  gating[i] = r1^2 * acos( (abs(d[i]) - 0.5*y2) / r1) -
              (abs(d[i])-0.5*y2)*sqrt( r1^2 - (abs(d[i])-0.5*y2)^2)
 else
  //Rectangle intersects circle
  gating[i] = (r1^2 * acos( (abs(d[i]) - 0.5*y2) / r1) -
              (abs(d[i])-0.5*y2)*sqrt(r1^2-(abs(d[i])-0.5*y2)^2)) -
              (r1^2 * acos( (abs(d[i]) + 0.5*y2) / r1) -
              (abs(d[i])+0.5*y2)*sqrt(r1^2-(abs(d[i])+0.5*y2)^2))
 endif
  gating[i] /= (pi*r1^2)
  timing[i] = d[i] / (2*pi*55.992*253)*1000
 //Write the TOF fit function:
 if (i < (numpnts(d) - 1))
  TMBstr += num2str(gating[i]) +
              "*(w[3]/(t-"+num2str(timing[i])+"-w[4]-delta))^4 *
              exp(-((w[3]/(t-"+num2str(timing[i])+"-w[4]-delta) -
              (w[3]/(w[5]-delta)))^2)/(alfa^2))+"
  else
  TMBstr += num2str(gating[i]) +
              "*(w[3]/(t-"+num2str(timing[i])+"-w[4]-delta))^4 *
              exp(-((w[3]/(t-"+num2str(timing[i])+"-w[4]-delta) -
              (w[3]/(w[5]-delta)))^2)/(alfa2̂))"
```

```
    endif
 endfor
 print TMBstr
End
```

Appendix **B**

Chapter 3

All experiments were performed in a homebuilt supersonic molecular beam ultra-high vacuum (UHV) apparatus. The base pressure of the UHV chamber is $<1{\cdot}10^{-10}$ mbar. The UHV chamber contains, amongst others, low energy electron diffraction (LEED) / Auger electron spectroscopy (AES) optics (BLD800IR, OCI Vacuum Microengineering), a quadrupole mass spectrometer (QME200, Pfeiffer vacuum) for residual gas analysis and King and Wells (KW) measurements, and an on-axis quadrupole mass spectrometer (UTI-100C) for time-of-flight (TOF) experiments.

The UHV chamber holds our curved Pt single crystal (Surface Preparation Lab). It is cooled using a liquid nitrogen cryostat and heated by radiative heating and electron bombardment using a filament. The Pt single crystal was cleaned with repeated cycles of sputtering ($6{\cdot}10^{-6}$ mbar Ar, Messer 5.0, 0.5 kV, 1.3 μA, 910 K, 50°, 5 min), oxidation ($3.5{\cdot}10^{-8}$ mbar O_2, Messer 5.0, 910 K), and *in vacuo* annealing (1200 K). For the final cleaning cycle, the Pt crystal is only sputtered and annealed at 910 K. Surface quality was verified using LEED and AES.

The double differentially pumped supersonic beam of D_2 is formed by expanding a gas mixture from a W nozzle with a 28 μm orifice. The center of the expansion is selected using a skimmer. A second skimmer and a sliding valve with different orifices create the molecular beam of variable size and shape within the UHV chamber. For the measurements, we use a slit as the defining orifice in the sliding valve. The molecular beam can be modulated by a mechanical chopper for time of flight spectroscopy or a pair of flags for King and Wells experiments.[11]

Time of Flight

The kinetic energy (E_{kin}) of the D_2 beam is varied by seeding in H_2 or anti-seeding in Ar. TOF spectra are measured at 6 different on-axis mass spectrometer positions. The resulting TOF spectra are fitted with the functional form for a density-sensitive detector:[54]

$$f(t) = \left(\frac{l}{t}\right)^4 \cdot e^{-\left(\frac{\frac{l}{t}-\frac{l}{t_0}}{\alpha}\right)^2} \tag{B.1}$$

where l is the neutral flight path, t is the neutral flight time, t_0 is the stream flight time and α is the width of the distribution. There are several offsets between the measured time and the actual neutral flight time. To determine the total offset, t_{offset}, TOF spectra are measured at 6 different QMS positions and fitted with a Gaussian function. We use linear regression on the resulting peak positions to extrapolate to $l = 0$ to extract $t = t_{offset}$. We subtract t_{offset} from the measured time, leaving only the neutral flight time t expressed in equation B.1. The TOF spectra are subsequently fitted with equation B.1. After redimensioning the fits using the appropriate Jacobian for transformation,[54] we obtain the two energy distributions in figure B.1.

Model 1 predictions

The predictions by model 1[61, 62] shown in figure 3.3 for the zero coverage limit are calculated by:

$$\tau = \frac{h}{k_B T_S} e^{\left(\frac{\eta E_W}{k_B T_s}\right)} \tag{B.2}$$

$$S_0 = S_{0nL} \frac{\nu\tau}{L_d} \left(1 - e^{\left(-\frac{L_d}{\nu\tau}\right)}\right) + 0.24\theta_d \tag{B.3}$$

The residence time τ depends on the precursor well depth E_W, and T_s. S_0 is the summation of two terms. The first term multiplies the probability of capture into the physisorbed state (S_{0nL}) with the probability of reaching a defect. The latter probability depends on τ, the incident velocity (ν), and the average distance between defects (L_d). The second term quantifies a minor contribution, i.e. the probability of dissociation through direct

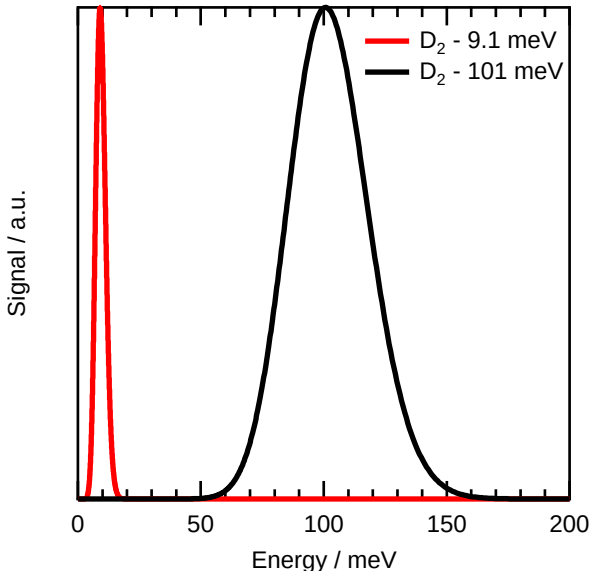

Figure B.1: Fitted flux-weighted energy distributions for the D_2 beams used in chapter 3, showing a most probable E_{kin} (FWHM) of 9.1 (4.7) meV and 101 (38) meV.

impact on defects. It equals 0.24 times the fractional defect density (θ_d). The fractional step density can be converted to step density in nm^{-1} by dividing by the Pt-Pt row distance for (1 1 1): 0.277 nm.[62] The value obtained for Pt(3 3 5) in this manner agrees with values used by Poelsema et al.[62] Besides Planck's constant (h), and Boltzmann's constant (k_B), the model requires an additional fit parameter (η) and assumes a θ_d dependence for E_W.[62]

The absolute values used in the model 1 predictions were extracted from the original publications by Poelsema et al.[61, 62] The values are shown in table B.1.

Table B.1: Model 1 simulation parameters.

S_{0nL}	0.09
η	$\frac{1}{1.35}$
E_W (eV)	$0.15L_d^{\left(\frac{0.13F}{N_A}\right)}$
L_d	$\frac{0.277}{\theta_D}$
ν	676.4 ms^{-1}
T_s	155 K or 300 K

Chapter 4

All experiments were performed in Lionfish; an ultra-high vacuum system described previously.[79] Hydrogen and deuterium were mixed with argon and expanded from a room temperature nozzle into the vacuum. Time of flight analysis was performed as described in chapter 2. The kinetic energy distributions resulting from fits to the data are shown in figure C.1 for H_2 and D_2.

Extracting results for the facetted surface

The experiments performed on the facetted Pt surface did not employ the standard King and Wells method. In contrast to the data presented in figure 4.1, the second beam flag (which resides in the UHV) remained open throughout the experiment. As a consequence, HD formation and D_2 consumption by the facetted Pt(1 1 1) surface cannot be extracted with the standard King and Wells[11] method detailed in chapter 2. For the facetted surface, we use the mass balance between consumed D_2 and produced HD for normalization. We explain our method in this section.

Figure C.2 shows the data for the reconstructed surface with the same temporal resolution as figure 4.1. First, we discuss the similarities to the raw data already shown in chapter 4. The measured D_2 pressure is highest at intermediate times, when the beam impinges near the (1 1 1) surface. In contrast, the HD pressure is high at the stepped surface at low and high relative times. There, measured D_2 pressures are somewhat lowered compared to the intermediate time. It is also clear that the sum of the HD and D_2 signal gradually increases throughout the experiment.

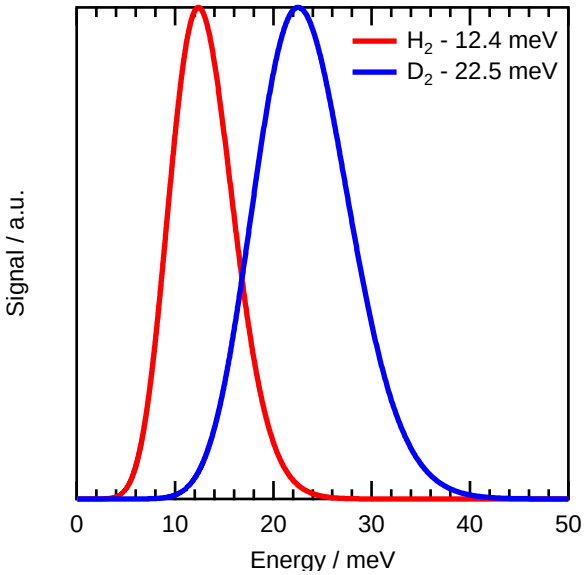

Figure C.1: H_2 and D_2 flux-weighted kinetic energy distributions determined from fits to the time of flight. The most probable E_{kin} (FWHM) for H_2 and D_2 are 12.4 (7.6) meV and 22.5 (11.4) meV respectively.

The experiments shown here exhibit significantly higher HD and D_2 pressures (approximately 20-30 times higher than for figure 4.1). This is a consequence of the larger slit size used to shape the molecular beam for these experiments (0.065 mm vs 0.250 mm). The beam is also open for a shorter period of time (12.5 s total compared to 30 s used previously). The biggest difference to the experiments shown in chapter 4 is that beam flag 2 remained open throughout the entire experiment. Due to missing the convenient normalization factor from scattering off the inert flag, we instead need to extract HD production and D_2 consumption probabilities by using the mass balance: the HD pressure increase is proportional to the D_2 pressure drop by the stoichiometry of the reaction. Variations in the ionization energy result in a change in the expected scaling factor. This scaling factor depends on the mass spectrometer settings and are best determined empirically. Fortunately, we have ample data for D_2 consumption and HD production to do this from the main experimental results in chapter 4.

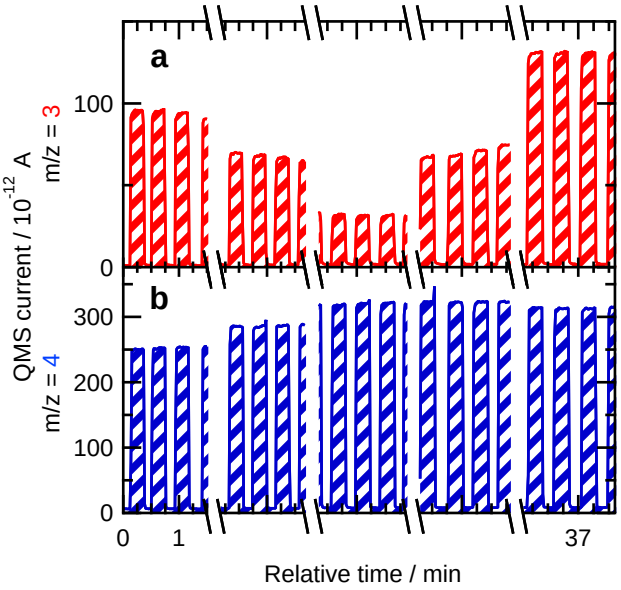

Figure C.2: The H_2-D_2 beam impinges different parts of the sample. From these data, structure dependent HD production and D_2 consumption are extracted.

Figure C.3 shows the drop in D_2 QMS current as a function of the increase in HD QMS current. A clear linear trend is observed. The slope represents the scaling factor between HD and D_2. Having determined the scaling factor, we calculate the total current attributed to D atoms present throughout the experiment and normalize to the initial total current. In addition, from the D_2, HD and total currents we calculate position (and step density) dependent D_2 consumption probabilities.

HD efficacy model

Chapter 4 detailed a simple model predicting HD selectivity at stepped Pt(1 1 1) surfaces. We explain here how equation 4.15 is calculated. We apply the same approach used for D_2 sticking in chapter 3 and Groot et al.[70] In chapter 4, we were left with:

$$\bar{S_0} = \alpha \cdot S_0^S + (1 - \alpha) \cdot S_0^T \tag{C.1}$$

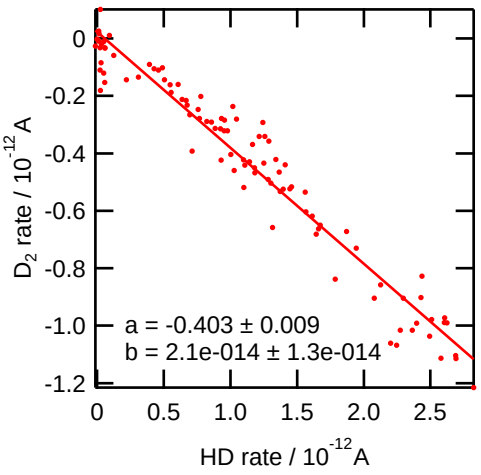

Figure C.3: Scaling between the D_2 pressure drop and the HD pressure increase.

and

$$\bar{C_0} = \frac{\alpha}{4} \cdot S_0^S + \left(\frac{1-\alpha}{2}\right) \cdot S_0^T \tag{C.2}$$

These are substituted into equation 4.11:

$$\eta = \frac{\frac{\alpha}{4} \cdot S_0^S + \left(\frac{1-\alpha}{2}\right) \cdot S_0^T}{\alpha \cdot S_0^S + (1-\alpha) \cdot S_0^T} \tag{C.3}$$

This can be simplified to the right hand side of equation 4.15 by realizing that:

$$S_0^S = 32 \cdot S_0^T \tag{C.4}$$

This results in:

$$\eta = \frac{\frac{\alpha}{4} \cdot 32 S_0^T + \left(\frac{1-\alpha}{2}\right) \cdot S_0^T}{\alpha \cdot 32 S_0^T + (1-\alpha) \cdot S_0^T} = \frac{8 \cdot \alpha + \frac{1}{2} - \frac{\alpha}{2} \cdot S_0^T}{32 \cdot \alpha + 1 - \alpha} = \frac{7.5 \cdot \alpha + \frac{1}{2}}{31 \cdot \alpha + 1} \tag{C.5}$$

To calculate α, we need to know what surface area can be considered a step edge or a terrace. To resolve this conundrum, we refer to our results in chapter 3. In chapter 3, we reported low energy D_2 sticking probabilities for the curved Pt(1 1 1) crystal. The results were fitted with a linear function, where the offset quantified reactivity at the (1 1 1) surface. We

showed that the slope represents the reaction cross section for the D_2 molecules impinging A- and B-type step edges. In chapter 4, we present a model that predicts HD formation as a function of step density. It assumes diffusive mixing at terraces and no diffusion at steps. We assume no exchange between the two different sites. Dissociation and HD exchange are governed by the relative abundance of step and terrace sites. Calculating the relative abundance of the terrace and step sites require the size of the step edge and the size of the unit cell. The latter can be calculated from the crystal position relative to the (1 1 1) surface. The first is determined from the reaction cross sections, by extrapolating our fits to reach unit sticking probability. Within error bars, extrapolated fits for A- and B-type steps closely resemble step densities for the (1 1 3) and (3 3 1) surface, respectively. These are surfaces that consist only of sites attributed to step edges and no terraces. Consequently, we describe the steps as {1 1 3} and {3 3 1} microfacets.

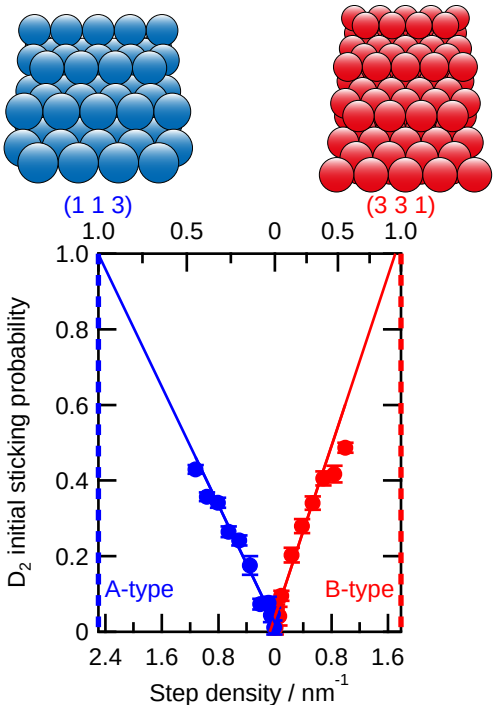

Figure C.4: Experimental fits from figure 3.2f extrapolated to (1 1 3) and (3 3 1). The top axis represent (1-α), showing the surface fraction that contributes to steps.

Appendix **D**

Chapter 5

Experiments were performed using Lionfish; an ultra-high vacuum (UHV) system with a base pressure lower than 10^{-10} mbar. The system is equipped with a double differentially pumped supersonic molecular beam (SSB), a single differentially pumped effusive beam (EB), a fixed quadrupole mass spectrometer (QMS, Balzers QMA 200), and a quadrupole mass spectrometer (UTI-100C) that can be translated along the SSB axis for time of flight measurements.

Forming the two molecular beams

The SSB is formed by expanding a constant flow (4 ml/min) of O_2 (Hoekloos, 5.0) from a tungsten nozzle with a 35 μm orifice. The expansion is subsequently shaped by two skimmers and an orifice, resulting in a 3.6 mm diameter circular oxygen beam (see chapter 2). The SSB can be modulated with two inert stainless steel beam flags and a mechanical chopper. The first differentially pumped stage houses the mechanical chopper, which is used for both reducing the amount of O_2 by the 16% duty cycle and time of flight experiments. Figure D.1 shows the kinetic energy distribution of the O_2 beam, as determined from fits to experimental data. The first O_2 flag is controlled using Labview and resides in the second differentially pumped stage. The second O_2 flag is a stepper motor controlled beam flag with a 50% duty cycle placed inside the UHV system. These O_2 beam flags are used in conjunction with two EB flags to perform King and Wells[11] type reactivity experiments between two or more reactants.

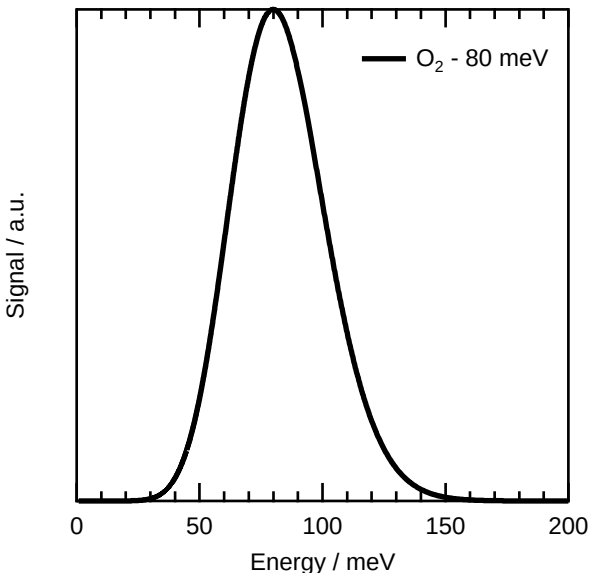

Figure D.1: Flux-weighted kinetic energy distribution of the O_2 supersonic beam, as determined from fits to the time of flight. The most probable E_{kin} (FWHM) is 80 (44) meV.

The effusive beam is formed by expanding varying flows (0.8-9.6 ml min^{-1}) of 1:1 mixed H_2:D_2 from a 0.2 mm nozzle. The beam is shaped by a skimmer and an orifice. The resulting hydrogen beam is approximately 7.7 mm in diameter at the sample and can be blocked by two beam flags. The first hydrogen flag is a manual gate valve that separates the differentially pumped stage from the UHV. Upon opening this flag, an effusive hydrogen load from the differentially pumped stage enters the UHV chamber. The second beam flag is a beam block on a manual rotation stage. This flag either blocks the hydrogen beam or admits it directly into the main chamber and onto the sample. H_2O and D_2O are contaminants in the UHV and the beam. In combination with the long vacuum time constant of water, this makes it challenging to even qualitatively measure that water formation occurs at our Pt samples. To partially circumvent this, we instead use a 1:1 mixture of H_2 and D_2 in the effusive beam. While HDO is also a contaminant in the beam, it is small compared to D_2O and H_2O

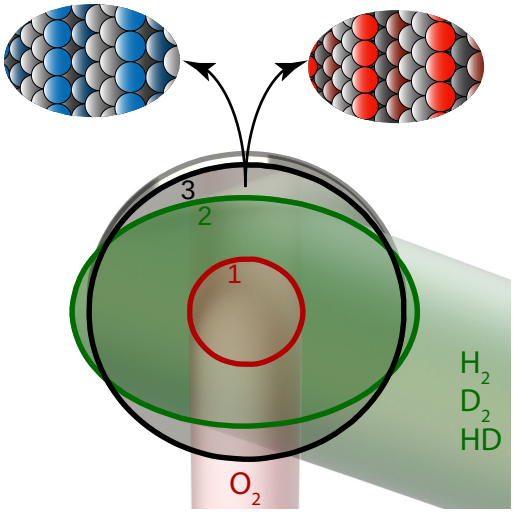

Figure D.2: Schematic overview of the experiment, where area 1 of the surface is pre-covered with the supersonic O_2 beam (red), and the effusive H_2/D_2 beam (green) subsequently reacts with the adsorbed oxygen. Experiments are performed on Pt(3 3 5) (left) and Pt(5 5 3) (right) surfaces at a surface temperature of 500 K.

since reactions in the background involving all three reactants - O_2, H_2, and D_2 - are less likely. The HDO signal shown here provides qualitative evidence of water formation.

Design of experiment

Figure D.2 schematically shows the experiment. The two molecular beams cross at 45° at the single crystal surface. The Pt(3 3 5) and Pt(5 5 3) crystals are 10 mm in diameter and cut and polished to within 0.1°. The crystals are oriented in the vacuum at normal incidence to the O_2 beam. The samples are cleaned by Ar sputtering (Messer, 5.0; 15 mA, 5 min.), oxidation (900 K, Messer, 5.0; $3.5{\cdot}10^{-8}$ mbar, 3 min.), and *in vacuo* annealing (1200 K) cycles. After each experiment, the sample is flashed to 1200 K to remove any remaining oxygen from the sample. Throughout the experiments, the surface temperature is regulated to 500 K.

Two typical experiments

Two typical experiments on Pt(3 3 5) are shown in figures D.3 and D.4. They are performed with excess hydrogen and excess oxygen, respectively. The four previously mentioned beam flags are manually operated at 30 s intervals. Panel a of figures D.3 and D.4 indicates the state of the oxygen and hydrogen flags. The effusive loads of the O_2 and hydrogen beams, resulting from the respective first flags, are shown as hatched red and hatched green backgrounds. The direct O_2 and hydrogen beams are depicted to scale in red and green respectively. The partial pressure of O_2, HD, and HDO are measured using the fixed QMS and presented in panels c, d, and e respectively. O-coverages are shown in panel b for guidance in the surface reactions at play. We estimate the initial maximum O-coverage by integrating the O_2 dissociative sticking results on the clean surface from 60-90 s, fitting it with an exponential function, and assuming 0.25 monolayers is reached upon extrapolating to its asymptote. The O-coverages throughout the remainder of the experiment are approximated from the coverage-dependent O_2 sticking. In the following sections, we will now explain the experiments in full and indicate notable features in the data.

0 - 120 s – O_2 sticking

At the start of each experiment, all flags are closed and both molecular beams are contained to their respective differentially pumped stages. Background pressures for O_2, HD, and HDO are measured for 30 s. First, oxygen is adsorbed to the surface in a standard King and Wells[11] type experiment. At 30 s, the first O_2 flag is retracted and the O_2 beam enters the main chamber. Upon entering the UHV, the O_2 beam scatters off the second O_2 flag and increases the background pressure. This is indicated in panel a with the red hatch. The second flag is retracted at 60 s. The O_2 beam directly impinges onto the sample, whereupon the O_2 partial pressure drops due to O_2 dissociative sticking. After covering the surface with O_{ads}, the second flag is closed at 90 s. The O_2 background signal returns to its original value. The modulated O_2 beam is well-suited

for measuring time-dependent sticking and determining the initial sticking probability. These are extracted by normalizing the measured pressure to the initial background pressure (t = 30-60 s), inverting, and subsequently signal-averaging with experiments performed under identical conditions. This yields the experimental results in figure 5.2.

120 - 210 s – Employing the H_2/D_2 beam

After (partially) covering the surface in oxygen (panel b) and measuring the background pressure for an additional 30 s, the effusive beam is employed at t = 120 s to react hydrogen with O_{ads}. Three notable things happen. First, the hydrogen beam is still contained to the differentially pumped stage, as shown in panel a. However, an effusive hydrogen flux already enters the UHV, as depicted by the green hatch in panel a. As a consequence of this hydrogen flux, the HD pressure in panel d increases. Second, the HDO pressure in panel e increases. Third, the O_2 pressure in panel c decreases. The effusive hydrogen flux reacts in the background, forming nascent HD and water. The background reaction with O_2 causes a fractional decrease in the O_2 QMS signal. As a consequence, O_2 sticking probabilities need to be calculated using O_2 background pressures measured under identical conditions, i.e. with the same hydrogen pressures.

In addition to background reactivity, the effusive hydrogen flux also reacts at the Pt surface. Throughout the experiment, the HD background pressure gradually increases. An additional increase in HD pressure is observed in excess hydrogen, exemplified by the inset at 157 s in figure D.3. The increase in HD pressure observed in the inset occurs earlier with increasing hydrogen flux. The HD pressure drops back to the initial level upon readsorbing O_2 at 180 s. Experiments that reveal this HD drop, also exhibit an O_2 sticking probability at 180 s that resembles the initial sticking probability for the clean surface. This shows that the O_{ads} was depleted in these experiments. In contrast, this increase in HD pressure is not observed for excess oxygen in figure D.4. The O_2 sticking probability at 180 s is lower than S_0 observed in figure 5.2, but higher than O_2 sticking

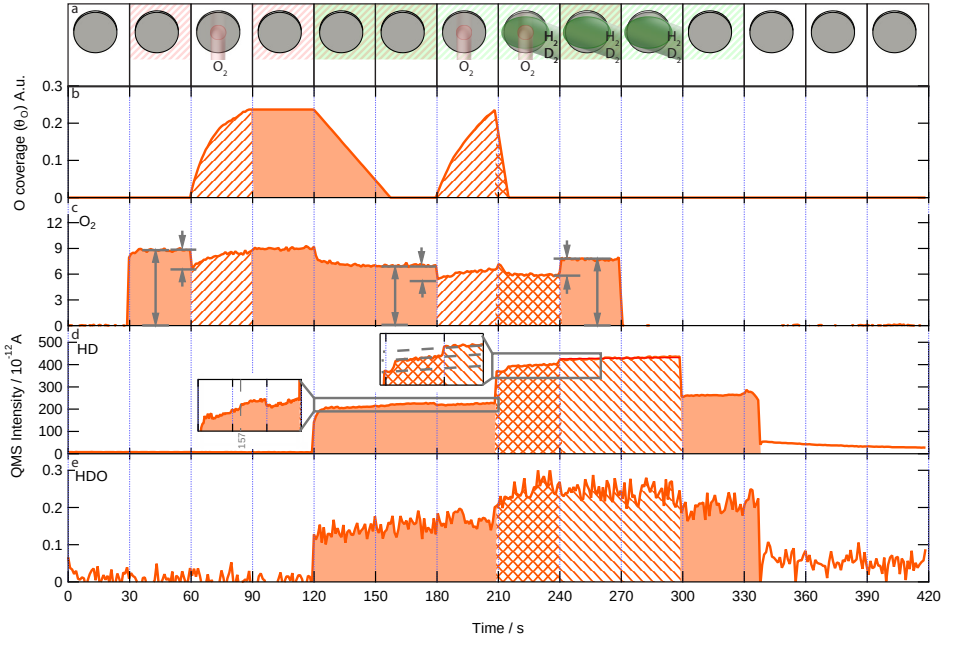

Figure D.3: Typical HDO formation experiment with excess hydrogen on Pt(3 3 5) at $T_s = 500$ K.

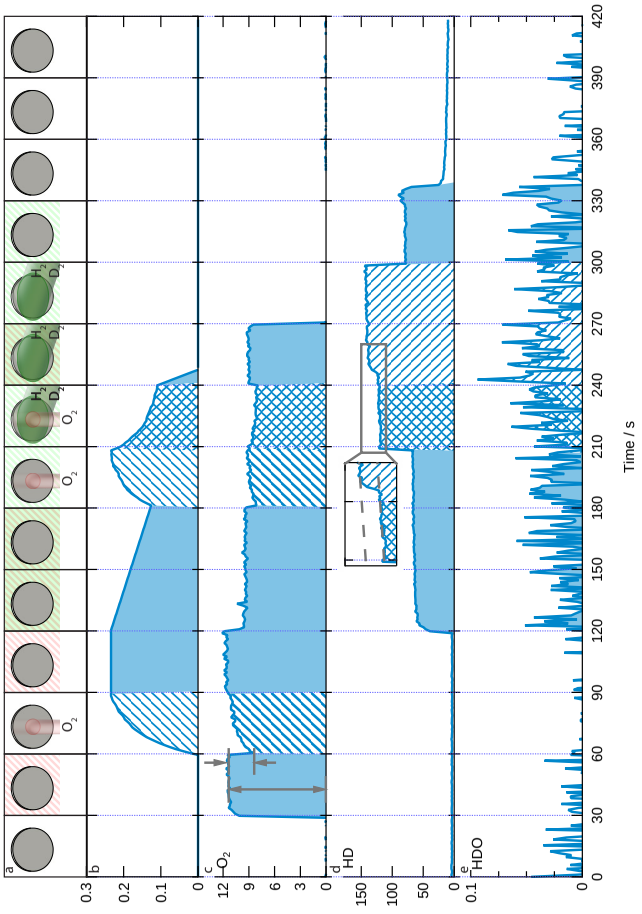

Figure D.4: Typical HDO formation experiment with limiting hydrogen on Pt(3 3 5) at $T_s = 500$ K.

at 150 s. Therefore, the O-coverage has decreased, but O_{ads} is not fully depleted. Consequently, we can already qualitatively state that reaction 5.1 occurs in the presence of O_{ads} and hydrogen at the expense of reaction 5.2.

The O_2 beam impinges onto the surface once more. The removed O_{ads} is replenished from 180 s until 210 s. O_2 sticking results measured at this point in the experiment are discussed in more detail in appendix D.

210 s – Direct reaction of O_2, H_2, and D_2

At 210 s, the second hydrogen flag is retracted. In figure 5.3, this point in the experiment is defined as time = 0. As indicated by panel a in figures D.3 and D.4, the oxygen and hydrogen beams both directly impinge onto the surface from 210 s until 240 s. Consequential to the incident hydrogen beam, three notable things occur.

First, the O_2 pressure in panel c increases upon impinging the hydrogen beam for high hydrogen fluxes, as shown in figure D.3, but remains the same for low hydrogen fluxes exemplified figure D.4. The O_2 pressure increase appears to result from a change in background reactivity, as indicated by the higher O_2 background pressure after 240 s than before 210 s in figure D.3.

Second, the HD pressure in panel d increases at 210 s due to reaction 5.2 from the hydrogen beam occuring in area 2 in figure D.2.

Third, the HDO pressure increases from two contributions. Additional HDO contamination enters the UHV chamber with the effusive beam or forms in the background. However, figure D.3 clearly shows a higher HDO pressure before 240 s than after. This qualitatively shows HDO forms at the Pt surface as a result of the O_2 and hydrogen beams. From 240 s onward, all valves are sequentially closed with the expected behavior for the partial pressure of O_2, HD, and HDO.

Analysis – HD deconvolution

At this point, we have given a full description of the different steps taken throughout the experiment. The most interesting features in the data are revealed by area 1 in figure D.2 — this is where O_2 reacts with H_2 and D_2. However, this is but a minor feature in the HD data. We now deconvolute the various contributions to the HD signal, so that we can extract reactivity in area 1 of figure D.2.

We start with the effusive flux that emerges from the effusive beam upon opening the EB1 gate valve at 120 s. Upon opening EB1, the EB2 beam flag remains closed until 210 s; i.e. the effusive beam does not yet enter the main chamber. The HD pressure increases significantly due to effusive load of H_2, D_2, and HD from the differentially pumped stage. The various contributions to this HD signal are disentangled in figure D.5. This effusive load consists of at least four separate contributions: HD contamination in the beam, HD formed in the expansion, HD formed in the UHV from various catalytic surfaces e.g. filaments, and HD formed by the sample. We quantify the first three by replacing the catalytically-active Pt surface with an inactive Au(1 1 1) surface, shown in dark gray. These contributions generate approximately 1/3 of the HD signal.

A clue to the influence of area 1 in figure D.2 is revealed at 140 s in figure D.5 and 157 s in the previously mentioned inset in figure D.3. There, the HD signal increases by approximately 4.4 % of the total amount. This 4.4% increase in HD partial pressure is observed for all relatively high flux H_2/D_2 beams on Pt(3 3 5). A similar increase is observed for Pt(5 5 3). Upon admitting oxygen to the sample at 180 s, the HD partial pressure instantaneously drops back to the initial pressure. This pressure drop is quantified and shown for both Pt(3 3 5) and Pt(5 5 3) in figure D.6. Additionally, the drop in HD appears independent of O-coverage. Three conclusions can be drawn from this behavior. First, dissociated hydrogen and deuterium are consumed by adsorbed oxygen, instead of forming HD. Second, the area covered by the oxygen beam is constant throughout the experiments.

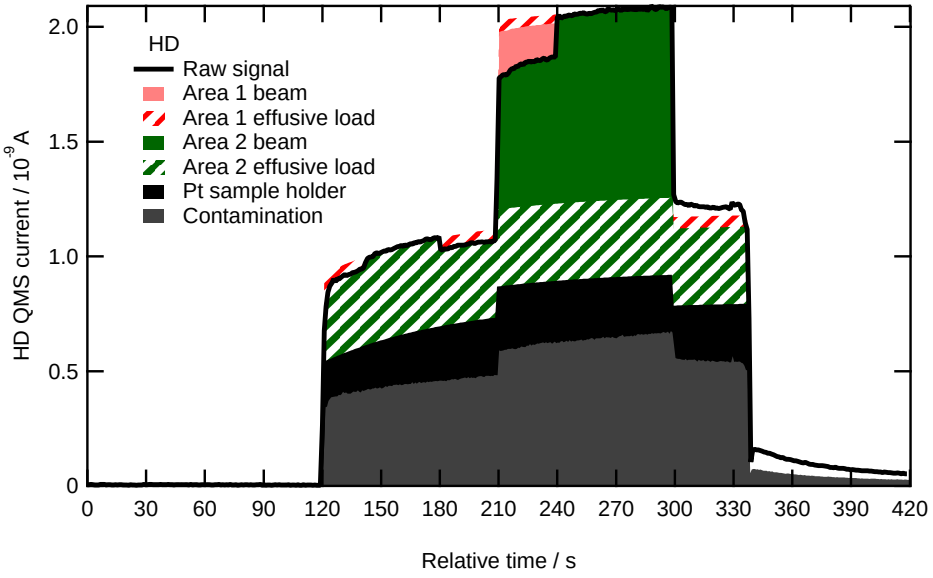

Figure D.5: The measured HD signal is convolved by various contributions that are generalized into contributions from the effusive load or the direct beam.

Third, the beam profile of the effusive beam is independent of flux. With these observations, HD produced by the sample can be disentangled by the following assumption: if (reactive) oxygen is present at the surface, adsorbed hydrogen reacts with oxygen to form water instead of recombinatively desorbing as HD.

This assumption first enables us to quantify the relative surface area of clean surface with respect to the O-covered surface — the sizes of which are independent of the oxygen or hydrogen flux. An effusive flux through an orifice should result in an isotropic hydrogen flux covering the entire sample and sample holder. Since the oxygen beam covers approximately 13% of the sample, the pressure drop is 13% (pink) of the total amount of HD produced by the sample (green) in figure D.5. This holds true for both the effusive flux (hatch) and direct beam (solid fill). A residual amount of HD is produced from a separate source not present in the Au(1 1 1)

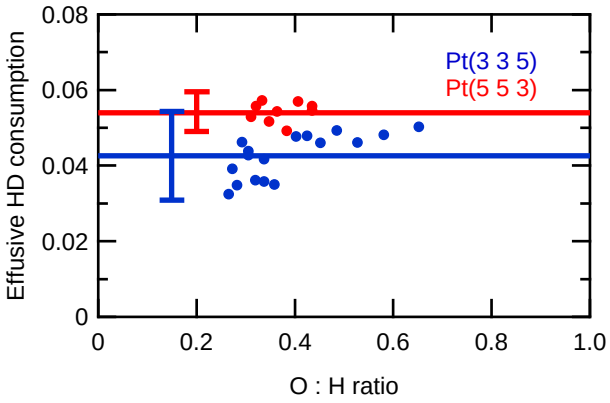

Figure D.6: Effusive HD pressure drop for different O:H ratios.

measurements (black) in figure D.5. This HD most likely forms on the side of sample or the Pt ribbon used to attach the sample to the sample holder.

Analysis - Area 1 reactivity

After deconvoluting the HD signal, we fully attribute changes in the HD pressure after t = 210 s to area 1 in figure D.2. For the hydrogen poor experiment in figure D.4, the HD pressure remains constant from 210 s until 245 s. In contrast, the hydrogen rich experiment in figure D.3 exhibits two HD pressure increases: at 215 s and 240 s. Here, the O_2 sticking probability quickly approximates S_0 in figure 5.2. We attribute the first observed pressure increase in figures D.3 and D.4 after 210 s to depletion of O_{ads}. Depletion of O_{ads} occurs while both molecular beams remain active for excess hydrogen in figure D.3 (see panel a). Consequently, a steady state sets in. There, all available O_{ads} from dissociative O_2 sticking is consumed first in reaction 5.1. Any remaining hydrogen recombinatively desorbs according to reactions 5.2. At 240 s, the O_2 beam stops directly impinging the sample and HD formation maximizes.

Figure D.7 presents an alternative view of figure 5.3 It includes the reaction probabilities before 210 s, i.e. before 0 s in figure 5.3. Panels a and b

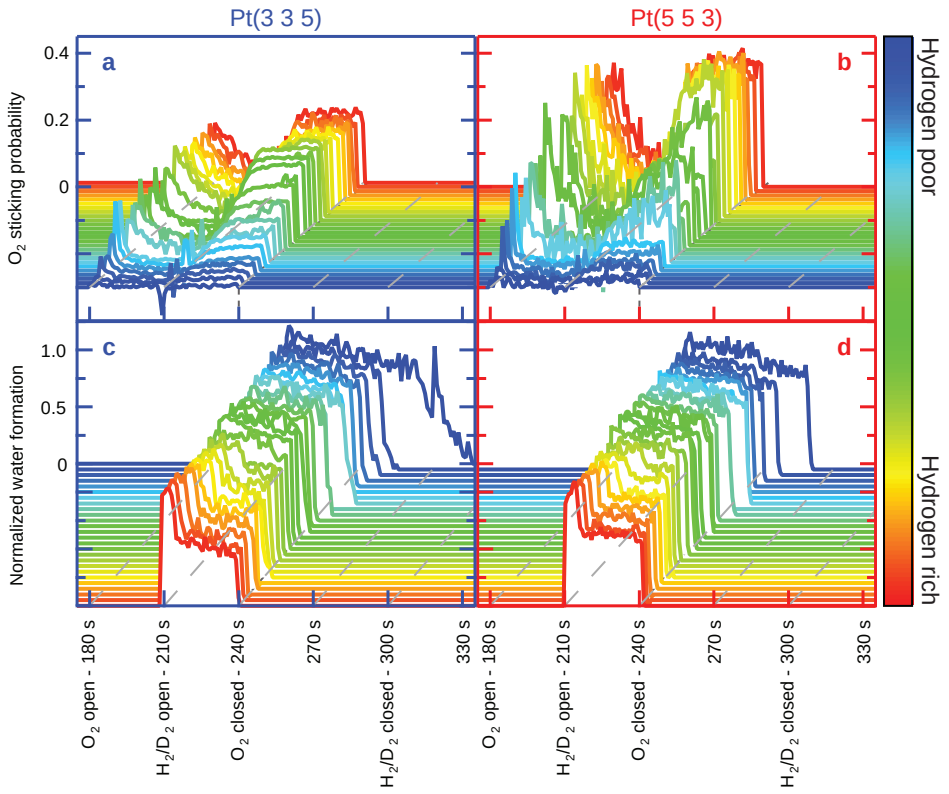

Figure D.7: Normalized water production, as measured from HD formation (see text), and O_2 consumption from the direct molecular beams in area 1 for Pt(3 3 5) (blue axes) and Pt(5 5 3) (red axes).

of figure D.7 show the O_2 sticking probability for Pt(3 3 5) and Pt(5 5 3) from 180 s onward, i.e. upon readmitting the O_2 beam. Two observations clearly point toward O_{ads} consumption by a surface reaction from hydrogen present in the background. First, dissociative O_2 sticking is clearly higher for both surfaces at 180 s than at t = 30 s in figure 5.2, showing that the O_{ads} coverage has lowered between 30 and 180 s. Second, the initial O_2 sticking probability at 180 s in figure D.7 increases with hydrogen flux. It is noteworthy that the O_2 sticking probabilities measured at 180 s are higher for Pt(5 5 3) than Pt(3 3 5), despite higher O-coverage for Pt(5 5 3). These data show that the Pt(5 5 3) surface with B-type step edges is more reactive under these conditions, despite Pt(5 5 3) having lower step density

than Pt(3 3 5). (0.96 nm^{-1} vs 1.13 nm^{-1}, respectively)

The O_{ads} coverage has replenished at 210 s after the O_2 beam has impinged onto the sample for 30 s, as indicated by the low O_2 sticking probabilities. The main results occur from 210 s onward and are elaborated on in chapter 5.

Extracting the O:H surface ratio

Figure D.7 already presents a wealth of information. Figure 5.3 makes an even more quantitative comparison by also plotting reactivity against the ratio of the reactive fluxes. Here, we explain how we extract the reactive flux ratio from the data. We define the reactive fluxes as the respective molecular fluxes multiplied with their initial sticking probabilitiy:

$$\begin{aligned} \phi_O &= 2S_{0,O_2} \cdot \phi_{O_2} \\ \phi_H &= 2S_{0,H_2} \cdot \phi_{H_2} \\ \phi_D &= 2S_{0,D_2} \cdot \phi_{D_2} \end{aligned} \tag{D.1}$$

where ϕ is the flux and S_0, i the sticking probability for molecule i. Absolute fluxes are challenging to extract, but the ratio of the reactive fluxes can be extracted directly from the data.

We have stated in chapter D that for the O_{ads} limited situation, a steady state situation sets in. In steady state, $\hat{R}_{H_2O}$ is a direct measure of the ratio of reactive O_2 and the H_2/D_2 fluxes. If we disregard any isotope dependencies, we may write this limiting reagent problem as:

$$2H_{ads} + \hat{R}_{H_2O} \cdot O_{ads} \rightarrow \hat{R}_{H_2O} \cdot H_2O + \left(1 - \hat{R}_{H_2O}\right) \cdot H_2 \tag{D.2}$$

The O_2 flow to the supersonic beam remains constant throughout the experiment. The O_2 beam is attenuated by chopping the beam with the mechanical chopper so that lower O:H ratio's could be achieved. We vary the relative flux of the two beams by changing the H_2/D_2 flow to the effusive beam using the flow controller. Chapter 2 showed that flux is proportional

to flow (and nozzle pressure) for the supersonic beam. We assume the same applies for the effusive beam, although scaling of flow and flux will differ compared to the supersonic molecular beam. Consequently, the flux ratio is proportional to the mass flow ratio applied by the flow controllers:

$$\dot{m}_{rel} = \frac{\dot{m}_{O_2}}{\dot{m}_{H_2} + \dot{m}_{D_2}} \propto \frac{\phi_{O_2}}{\phi_{D_2} + \phi_{H_2}} \tag{D.3}$$

where $\dot{m}_i$ and ϕ_i are the flow and flux of compound i respectively. $\hat{R}_{H_2O}$ requires including the reaction probabilities. Under O_{ads} limited steady state conditions, the O-coverage is low and reaction probabilities resemble that of the clean surface. Under these conditions, the relative molecular fluxes scale with the relative reactive fluxes:

$$\frac{\phi_{O_2}}{\phi_{D_2} + \phi_{H_2}} \propto \frac{S_{0,O_2}\phi_{O_2}}{S_{0,D_2}\phi_{D_2} + S_{0,H_2}\phi_{H_2}} \tag{D.4}$$

Figure D.8 compares the $\hat{R}_{H_2O}$ with the relative flow, $\dot{m}_{rel}$, and confirms our premise that $\hat{R}_{H_2O}$ in steady state is proportional to the relative oxygen flow. While the measured $\hat{R}_{H_2O}$ cannot exceed 1, the actual O:H ratio can. We use least squares fitting for the Pt(3 3 5) and Pt(5 5 3) data in figure D.8. Subsequently, we extract the scaling between $\hat{R}_{H_2O}$ and the relative flow under the O_{ads} limited steady state condition, i.e. where O_2 sticking is constant. We then extrapolate the fit to excess O_2 data, where θ_O exceeds 0, to allows us to quantify the relative fluxes shown by equation D.4. We emphasize here that higher O_2 sticking for Pt(5 5 3) than Pt(3 3 5) is incorporated in the O:H ratio; the slope for Pt(5 5 3) exceeds that of Pt(3 3 5) in figure D.8.

Additional evidence of increased hydrogen reactivity

While we measure O_2 sticking directly, we did not do the same for hydrogen or deuterium. We disregard isotope effects in the following discussion. However, the slopes presented in figure D.8 provide clues to the reactivity differences. As shown by equation D.4, the slopes in figure D.8 are a direct consequence of the O_2 reactive flux and the H_2 and D_2 reactive fluxes. If we assume the molecular fluxes are identical for the two experiments, then any

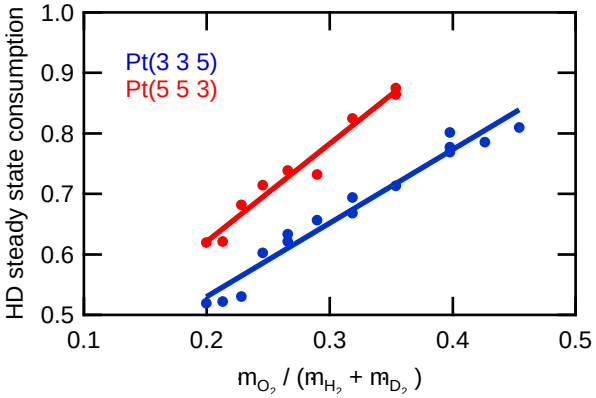

Figure D.8: HD consumption at steady state.

difference in slope in figure D.8 is a consequence of the sticking probabilities. With 0.35 compared to 0.25, the initial O_2 sticking probability for Pt(5 5 3) exceeds that of Pt(3 3 5).

An interesting observation may be made here: the ratio of the slopes in figure D.8 is lower than the O_2 S_0 ratio, with 1.33 compared to 1.4. Error bars may be partially responsible for the difference. If we ignore error bars, this also suggests that hydrogen is more reactive at Pt(5 5 3) than Pt(3 3 5) under these conditions. We explain our reasoning.

The slopes are described by the right hand side of equation D.4. The ratio of the two slopes then represent:

$$\frac{\left(\frac{S^{5\ 5\ 3}_{0,O_2}\phi_{O_2}}{S^{5\ 5\ 3}_{0,D_2}\phi_{D_2}+S^{5\ 5\ 3}_{0,H_2}\phi_{H_2}}\right)}{\left(\frac{S^{3\ 3\ 5}_{0,O_2}\phi_{O_2}}{S^{3\ 3\ 5}_{0,D_2}\phi_{D_2}+S^{3\ 3\ 5}_{0,H_2}\phi_{H_2}}\right)} = 1.33 \tag{D.5}$$

The relative flows, and hence the molecular fluxes, used in the experiment are identical. If we simplify the equation and assume no isotope dependence

for S_0 for H_2:

$$\frac{\left(\frac{S^{5\ 5\ 3}_{0,O_2}}{S^{5\ 5\ 3}_{0,H_2}}\right)}{\left(\frac{S^{3\ 3\ 5}_{0,O_2}}{S^{3\ 3\ 5}_{0,H_2}}\right)} = 1.33 \tag{D.6}$$

From the data in figure 5.2, we extracted S_0 for the A- and B-type surfaces of 0.25 and 0.35. respectively. Substitution and isolation of the hydrogen reactivity yields:

$$\frac{S^{3\ 3\ 5}_{0,H_2}}{S^{5\ 5\ 3}_{0,H_2}} = \frac{S^{5\ 5\ 3}_{0,O_2}}{S^{3\ 3\ 5}_{0,O_2}} \cdot 1.33 = 0.95 \tag{D.7}$$

These results suggest that Pt(5 5 3) is 5% more reactive for hydrogen dissociation. Higher reactivity for Pt(5 5 3) than Pt(3 3 5) qualitatively agrees with our previous results on D_2 dissociation. However, the results presented here assumes that the O_2 flux was equal for both experiments. The experiments for Pt(3 3 5) and Pt(5 5 3) were measured 7 months apart. While the same O_2 flow was applied to the nozzle during the experiments, the nozzle pressure increased from the Pt(5 5 3) experiments to the Pt(3 3 5) experiments. We do not believe the flux was affected, but cannot completely rule it out either. The O:H ratio is unaffected as these are calculated from the separate data sets. Similarity of the data suggests that the absolute fluxes were similar.

Bibliography

[1] Davy, H. *Philos. Trans. R. Soc.* **107**, 77–85 (1817).

[2] Berzelius, J. J. *Ann. Chim. Phys.* **61**, 146–151 (1836).

[3] Henry, W. *Philos. Trans. R. Soc.* **114**, 266–289 (1824).

[4] Brønsted, J. N. and Pedersen, K. *Z. Phys. Chem. Stoechiom. Verwandtschaftsl.* **108**(185) (1924).

[5] Langmuir, I. *Nobel Lectures* (1932).

[6] Davisson, C. J. and Germer, L. H. *Proc. Natl. Acad. Sci. U.S.A.* **14**, 317–322 (1928).

[7] de Broglie, L. *Recherches sur la théorie des quanta.* PhD thesis, Université Paris-Sorbonne, (1924).

[8] Davisson, C. and Germer, L. H. *Phys. Rev.* **30**, 705–740 (1927).

[9] Davisson, C. *Nobel Lectures* (1937).

[10] Stern, O. *Nobel Lectures* (1946).

[11] King, D. A. and Wells, M. G. *Surf. Sci.* **29**, 454–482 (1972).

[12] Auerbach, D. J., Pfnür, H. E., Rettner, C. T., Schlaegel, J. E., Lee, J., and Madix, R. J. *J. Chem. Phys.* **81**, 2515–2516 (1984).

[13] D´evelyn, M. P., Hamza, A. V., Gdowski, G. E., and Madix, R. J. *Surf. Sci.* **167**, 451–473 (1986).

[14] Luntz, A. C., Williams, M. D., and Bethune, D. S. *J. Chem. Phys.* **89**, 4381–4395 (1988).

[15] Lee, M. B., Yang, Q. Y., Tang, S. L., and Ceyer, S. T. *J. Chem. Phys.* **85**, 1693–1694 (1986).

[16] Rettner, C. T., Pfnür, H. E., and Auerbach, D. J. *Phys. Rev. Lett.* **54**, 2716–2719 (1985).

[17] Rettner, C. T., Pfnür, H. E., and Auerbach, D. J. *J. Chem. Phys.* **84**, 4163–4167 (1986).

[18] Luntz, A. C., Brown, J. K., and Williams, M. D. *J. Chem. Phys.* **93**, 5240–5246 (1990).

[19] Gostein, M., Parhikhteh, H., and Sitz, G. O. *Phys. Rev. Lett.* **75**, 342–345 (1995).

[20] Juurlink, L. B. F., McCabe, P. R., Smith, R. R., DiCologero, C. L., and Utz, A. L. *Phys. Rev. Lett.* **83**, 868–871 (1999).

[21] Hundt, P. M., Jiang, B., van Reijzen, M. E., Guo, H., and Beck, R. D. *Science* **344**(6183), 504–507 (2014).

[22] Juurlink, L. B. F., Killelea, D. R., and Utz, A. L. *Prog. Surf. Sci.* **84**, 69–134 (2009).

[23] Beck, R. D., Maroni, P., Papageorgopoulos, D. C., Dang, T. T., Schmid, M. P., and Rizzo, T. R. *Science* **302**(5642), 98–100 (2003).

[24] Killelea, D. R., Campbell, V. L., Shuman, N. S., and Utz, A. L. *Science* **319**, 790–793 (2008).

[25] Kurahashi, M. and Yamauchi, Y. *Phys. Rev. B* **85**, 161302 (2012).

[26] Ueta, H. and Kurahashi, M. *Angew. Chem. Int. Ed.* **56**, 4174–4177 (2017).

[27] Cao, K., van Lent, R., Kleyn, A. W., Kurahashi, M., and Juurlink, L. B. F. *Proc. Natl. Acad. Sci. U.S.A.* **116**, 13862–13866 (2019).

[28] Somorjai, G. A. *Catal. Lett.* **7**(1-4), 169 (1990).

[29] Vattuone, L., Savio, L., and Rocca, M. *Surf. Sci. Rep.* **63**, 101–168 (2008).

[30] Hahn, C., Shan, J., Liu, Y., Berg, O., Kleyn, A. W., and Juurlink, L. B. F. *J. Chem. Phys.* **136**, 114201 (2012).

[31] Veser, G., Thiel, P. A., and Imbihl, R. *J. Phys. Chem.* **98**, 2148–2151 (1994).

[32] Sander, M., Imbihl, R., and Ertl, G. *J. Chem. Phys.* **97**, 5193–5204 (1992).

[33] Lawton, T. J., Pushkarev, V., Wei, D., Lucci, F. R., Sholl, D. S., Gellman, A. J., and Sykes, E. C. H. *J. Phys. Chem. C* **117**, 22290–22297 (2013).

[34] Gellman, A. J., Tysoe, W. T., and Zaera, F. *Catal. Lett.* **145**, 220–232 (2015).

[35] Mom, R. V., Hahn, C., Jacobse, L., and Juurlink, L. B. F. *Surf. Sci.* **613**, 15–20 (2013).

[36] Walter, A. L., Schiller, F., Corso, M., Merte, L. R., Bertram, F., Lobo-Checa, J., Shipilin, M., Gustafson, J., Lundgren, E., Bríón-Ríos, A. X., Cabrera-Sanfelix, P., Sánchez-Portal, D., and Ortega, J. E. *Nat. Commun.* **6**, 8903 (2015).

[37] Janlamool, J., Bashlakov, D., Berg, O., Praserthdam, P., Jongsomjit, B., and Juurlink, L. B. F. *Molecules* **19**, 10845–10862 (2014).

[38] Arulmozhi, N., Esau, D., Lamsal, R. P., Beauchemin, D., and Jerkiewicz, G. *ACS Catal.* **8**, 6426–6439 (2018).

[39] Besocke, K., Krahl-Urban, B., and Wagner, H. *Surf. Sci.* **68**, 39–46 (1977).

[40] Liu, H. T., Armitage, A. F., and Woodruff, D. P. *Surf. Sci.* **114**, 431–444 (1982).

[41] Armitage, A. F., Liu, H. T., and Woodruff, D. P. *Vacuum* **31**, 519–522 (1981).

[42] Corso, M., Schiller, F., Fernández, L., Cordón, J., and Ortega, J. E. *J. Phys. Condens. Matter* **21**(35), 353001 (2009).

[43] De Alwis, A., Holsclaw, B., Pushkarev, V. V., Reinicker, A., Lawton, T. J., Blecher, M. E., Sykes, E. C. H., and Gellman, A. J. *Surf. Sci.* **608**, 80–87 (2013).

[44] Ortega, J. E., Corso, M., Abd-el Fattah, Z. M., Goiri, E. A., and Schiller, F. *Phys. Rev. B* **83**, 085411 (2011).

[45] Blomberg, S., Zetterberg, J., Zhou, J., Merte, L. R., Gustafson, J., Shipilin, M., Trinchero, A., Miccio, L. A., Magaña, A., Ilyn, M., Schiller, F., Ortega, J. E., Bertram, F., Grönbeck, H., and Lundgren, E. *ACS Catal.* **7**, 110–114 (2017).

[46] Füchsel, G., Cao, K., Er, S., Smeets, E. W. F., Kleyn, A. W., Juurlink, L. B. F., and Kroes, G. J. *J. Phys. Chem. Lett.* **9**, 170–175 (2018).

[47] Neugebohren, J., Borodin, D., Hahn, H. W., Altschäffel, J., Kandratsenka, A., Auerbach, D. J., Campbell, C. T., Schwarzer, D., Harding, D. J., Wodtke, A. M., and Kitsopoulos, T. N. *Nature* **558**, 280–283 (2018).

[48] Chadwick, H., Guo, H., Gutiérrez-González, A., Menzel, J. P., Jackson, B., and Beck, R. D. *J. Chem. Phys.* **148**, 014701 (2018).

[49] Bernasek, S. L., Siekhaus, W. J., and Somorjai, G. A. *Phys. Rev. Lett.* **30**, 1202–1204 (1973).

[50] Lang, B., Joyner, R. W., and Somorjai, G. A. *Surf. Sci.* **30**, 440–453 (1972).

[51] van der Niet, M. J. T. C., den Dunnen, A., Juurlink, L. B. F., and Koper, M. T. M. *J. Chem. Phys.* **132**, 174705 (2010).

[52] Weisstein, E. W. `http://mathworld.wolfram.com/Circle-CircleIntersection.html`. Accessed: 2019-09-05.

[53] Cao, K. *Structure dependence of molecular reactions on surfaces.* PhD thesis, Leiden University, (2018).

[54] Auerbach, D. J. In *in Atomic Molecular Beam Methods,* Scoles, G., editor, chapter 14, 362–379. Oxford Univ. Press, Oxford (1988).

[55] Haberland, H., Buck, U., and Tolle, M. *Review of Scientific Instruments* **56**, 1712–1716 (1985).

[56] Groot, I. M. N. *The fight for a reactive site.* PhD thesis, Leiden University, (2009).

[57] Gergen, B., Nienhaus, H., Weinberg, W. H., and McFarland, E. W. *Science* **294**, 2521–2523 (2001).

[58] Meyer, J. and Reuter, K. *Angew. Chemie Int. Ed.* **53**, 4721–4724 (2014).

[59] Kroes, G. J. *Science* **321**(5890), 794–797 (2008).

[60] Diaz, C., Pijper, E., Olsen, R. A., Busnego, H. F., Auerbach, D. J., and Kroes, G. J. *Science* **326**, 832–834 (2009).

[61] Poelsema, B., Lenz, K., and Comsa, G. *J. Phys. Condens. Matter* **30**(22), 304006 (2010).

[62] Poelsema, B., Lenz, K., and Comsa, G. *J. Chem. Phys.* **134**, 074703 (2011).

[63] Cowin, J. P., Yu, C. F., Sibener, S. J., and Wharton, L. *J. Chem. Phys.* **79**, 3537–3549 (1983).

[64] Sanz, A. S. and Miret-Artés, S. *Phys. Rep.* **451**, 37–154 (2007).

[65] McCormack, D. A., Olsen, R. A., and Baerends, E. J. *J. Chem. Phys.* **122**(19), 194708 (2005).

[66] Gee, A. T., Hayden, B. E., Mormiche, C., and Nunney, T. S. *J. Chem. Phys.* **112**, 7660–7668 (2000).

[67] Salmeron, M., Gale, R. J., and Somorjai, G. A. *J. Chem. Phys.* **67**, 5324–5334 (1977).

[68] Groot, I. M. N., Schouten, K. J. P., Kleyn, A. W., and Juurlink, L. B. F. *J. Chem. Phys.* **129**, 224707 (2008).

[69] Groot, I. M. N., Kleyn, A. W., and Juurlink, L. B. F. *Angew. Chemie Int. Ed.* **50**, 5174–5177 (2011).

[70] Groot, I. M. N., Kleyn, A. W., and Juurlink, L. B. F. *J. Phys. Chem. C* **117**, 9266–9274 (2013).

[71] Walsh, A. J., van Lent, R., Auras, S. V., Gleeson, M. A., Berg, O. T., and Juurlink, L. B. F. *J. Vac. Sci. Technol. A Vacuum, Surfaces, Film.* **35**(3), 03E102 (2017).

[72] Samson, P., Nesbitt, A., Koel, B. E., and Hodgson, A. *J. Chem. Phys.* **109**, 3255–3264 (1998).

[73] Nour Ghassemi, E., Wijzenbroek, M., Somers, M. F., and Kroes, G. J. *Chem. Phys. Lett.* **683**, 329–335 (2017).

[74] Cao, K., van Lent, R., Kleyn, A. W., and Juurlink, L. B. F. *Chem, Phys. Lett.* **706**, 680–683 (2018).

[75] Luppi, M., McCormack, D. A., Olsen, R. A., and Baerends, E. J. *J. Chem. Phys.* **123**(16), 164702 (2005).

[76] Lu, K. E. and Rye, R. R. *Surf. Sci.* **45**, 677–695 (1974).

[77] Christmann, K., Ertl, G., and Pignet, T. *Surf. Sci.* **54**, 365–392 (1976).

[78] Salmeron, M., Gale, R. J., and Somorjai, G. A. *J. Chem. Phys.* **70**(6), 2807 (1979).

[79] van Lent, R., Auras, S. V., Cao, K., Walsh, A. J., Gleeson, M. A., and Juurlink, L. B. F. *Science* **363**(6423), 155–157 (2019).

[80] Christmann, K. and Ertl, G. *Surf. Sci.* **60**, 365–384 (1976).

[81] Graham, A. P., Menzel, A., and Toennies, J. P. *J. Chem. Phys.* **111**, 1676–1685 (1999).

[82] Kristinsdóttir, L. and Skúlason, E. *Surf. Sci.* **606**, 1400–1404 (2012).

[83] Olsen, R. A., Kroes, G. J., and Baerends, E. J. *J. Chem. Phys.* **111**, 11155–11163 (1999).

[84] Jardine, A. P., Lee, E. Y. M., Ward, D. J., Alexandrowicz, G., Hedgeland, H., Allison, W., Ellis, J., and Pollak, E. *Phys. Rev. Lett.* **105**, 136101 (2010).

[85] Bădescu, Ş. C., Salo, P., Ala-Nissila, T., Ying, S. C., Jacobi, K., Wang, Y., Bedürftig, K., and Ertl, G. *Phys. Rev. Lett.* **88**, 136101 (2002).

[86] Zheng, C. Z., Yeung, C. K., Loy, M. M. T., and Xiao, X. *Phys. Rev. B* **70**, 205402 (2004).

[87] Zheng, C. Z., Yeung, C. K., Loy, M. M. T., and Xiao, X. *Phys. Rev. Lett.* **97**, 166101 (2006).

[88] Olsen, R. A., Bădescu, Ş. C., Ying, S. C., and Baerends, E. J. *J. Chem. Phys.* **120**, 11852–11863 (2004).

[89] Hahn, E., Schief, H., Marsico, V., Fricke, A., and Kern, K. *Phys. Rev. Lett.* **72**, 3378–3381 (1994).

[90] den Dunnen, A. *Surface-structure dependencies in catalytic reactions.* PhD thesis, Leiden University, (2015).

[91] Comsa, G., Mechtersheimer, G., and Poelsema, B. *Surf. Sci.* **97**(1), L297 – L303 (1980).

[92] Balmes, O., Prevot, G., Torrelles, X., Lundgren, E., and Ferrer, S. *ACS Catal.* **6**(2), 1285–1291 (2016).

[93] Calle-Vallejo, F., Loffreda, D., Koper, M. T. M., and Sautet, P. *Nat. Chem.* **7**, 403–410 (2015).

[94] Calle-Vallejo, F., Tymoczko, J., Colic, V., Vu, Q. H., Pohl, M. D., Morgenstern, K., Loffreda, D., Sautet, P., Schuhmann, W., and Bandarenka, A. S. *Science* **350**, 185–189 (2015).

[95] Stephens, I. E. L., Bondarenko, A. S., Grønbjerg, U., Rossmeisl, J., and Chorkendorff, I. *Energy Environ. Sci.* **5**, 6744–6762 (2012).

[96] Ertl, G. *Angew. Chem. Int. Ed.* **47**(19), 3524–3535 (2008).

[97] Nørskov, J. K., Bligaard, T., Logadottir, A., Bahn, S., Hansen, L. B., Bollinger, M., Bengaard, H., Hammer, B., Sljivancanin, Z., Mavrikakis, M., Xu, Y., Dahl, S., and Jacobsen, C. J. H. *J. Catal.* **209**(2), 275–278 (2002).

[98] Verheij, L. K. and Hugenschmidt, M. B. *Surf. Sci.* **416**(1-2), 37–58 (1998).

[99] Michely, T. and Comsa, G. *Surf. Sci.* **256**, 217 – 226 (1991).

[100] Bondü, C. J., Calle-Vallejo, F., Figueiredo, M. C., and Koper, M. T. M. *Nat. Catal.* **2**, 243–250 (2019).

[101] Gee, A. T. and Hayden, B. E. *J. Chem. Phys.* **113**, 10333–10343 (2000).

[102] Jacobse, L., den Dunnen, A., and Juurlink, L. B. F. *J. Chem. Phys.* **143**, 014703 (2015).

[103] van der Niet, M. J. T. C., den Dunnen, A., Juurlink, L. B. F., and Koper, M. T. M. *Angew. Chem. Int. Ed.* **49**(37), 6572–6575 (2010).

[104] Verheij, L. K., Hugenschmidt, M. B., Poelsema, B., and Comsa, G. *Surf. Sci.* **233**, 209–222 (1990).

[105] Gee, A. T., Hayden, B. E., Mormiche, C., and Nunney, T. S. *Surf. Sci.* **512**(3), 165–172 (2002).

[106] Honkala, K., Hellman, A., Remediakis, I. N., Logadottir, A., Carlsson, A., Dahl, S., Christensen, C. H., and Nørskov, J. K. *Science* **307**, 555–558 (2005).

[107] Behrens, M., Studt, F., Kasatkin, I., Kühl, S., Hävecker, M., Abild-Pedersen, F., Zander, S., Girgsdies, F., Kurr, P., Kniep, B.-L., Tovar, M., Fischer, R. W., Nørskov, J. K., and Schlögl. *Science* **336**(6083), 893–897 (2012).

[108] Hoffmann, F. M. *Surf. Sci. Rep.* **3**, 107–192 (1983).

[109] Chabal, Y. J. *Surf. Sci. Rep.* **8**(5-7), 211–357 (1988).

[110] Greenler, R. G. *J. Chem. Phys.* **50**, 1963 (1969).

[111] Greenler, R. G. *J. Chem. Phys.* **44**(1), 310–315 (1966).

[112] Suzaki, Y. and Tachibana, A. *Appl. Opt.* **14**, 2809–2810 (1975).

[113] Ertl, G. *Reactions at solid surfaces*, volume 14. John Wiley & Sons, (2010).

[114] McEwen, J.-S., Payne, S. H., Kreuzer, H. J., Kinne, M., Denecke, R., and Steinrück, H.-P. *Surf. Sci.* **545**, 47–69 (2003).

[115] Steininger, H., Lehwald, S., and Ibach, H. *Surf. Sci.* **123**(2-3), 264–282 (1982).

[116] Baro, A. M. and Ibach, H. *J. Chem. Phys.* **71**, 4812 (1979).

[117] Ogletree, D. F., Van Hove, M. A., and Somorjai, G. A. *Surf. Sci.* **173**, 351–365 (1986).

[118] Ertl, G., Neumann, M., and Streit, K. M. *Surf. Sci.* **64**(2), 393–410 (1977).

[119] Yang, H. J., Minato, T., Kawai, M., and Kim, Y. *J. Phys. Chem. C* **117**, 16429–16437 (2013).

[120] Ryberg, R. *Phys. Rev. B* **40**(1), 865 (1989).

[121] Malik, I. J. and Trenary, M. *Surf. Sci. Lett.* **214**, L237–L245 (1989).

[122] Xu, J. and Yates, J. T. *Surf. Sci.* **327**, 193–201 (1995).

[123] Mukerji, R. J., Bolina, A. S., and Brown, W. A. *Surf. Sci.* **527**, 198–208 (2003).

[124] Tränkenschuh, B., Fritsche, N., Fuhrmann, T., Papp, C., Zhu, J. F., Denecke, R., and Steinrück, H.-P. *J. Chem. Phys.* **124**(7), 074712 (2006).

[125] Tränkenschuh, B., Papp, C., Fuhrmann, T., Denecke, R., and Steinrück, H.-P. *Surf. Sci.* **601**, 1108–1117 (2007).

[126] Shimizu, S., Noritake, H., Koitaya, T., Mukai, K., Yoshimoto, S., and Yoshinobu, J. *Surf. Sci.* **608**, 220–225 (2013).

[127] van Hove, M. A. and Somorjai, G. A. *Surf. Sci.* **92**, 489 (1980).

[128] Yoshinobu, J., Tsukahara, N., Yasui, F., Mukai, K., and Yamashita, Y. *Phys. Rev. Lett.* **90**, 248301 (2003).

[129] Blyholder, G. *J. Phys. Chem.* **68**(10), 2772–2777 (1964).

[130] Crossley, A. and King, D. A. *Surf. Sci.* **68**, 528–538 (1977).

[131] Horn, K. and Pritchard, J. *J. Phys. Colloq.* **38**(C4), 164–171 (1977).

[132] Hollins, P. *Surf. Sci. Rep.* **16**, 51–94 (1992).

[133] Froitzheim, H., Hopster, H., Ibach, H., and Lehwald, S. *Appl. Phys.* **13**, 147–151 (1977).

[134] Herzberg, G. *Molecular spectra and molecular structure, vol II.* Van Nostrand Reinhold Company, (1945).

[135] Nagaoka, S. I., Teramae, H., and Nagashima, U. *J. Chem. Educ.* **90**, 669–670 (2013).

[136] Yoder, B. L. *Steric Effects in the Chemisorption of Vibrationally Excited Methane on Nickel*. PhD thesis, L´Ecole Polytechnique Fédérale de Lausanne, (2012).

[137] Rothman, L. S., Gordon, I. E., Barbe, A., Benner, D. C., Bernath, P. F., Birk, M., Boudon, V., Brown, L. R., Campargue, A., Champion, J. P., Chance, K., Coudert, L. H., Dana, V., Devi, V. M., Fally, S., Flaud, J. M., Gamache, R. R., Goldman, A., Jacquemart, D., Kleiner, I., Lacome, N., Lafferty, W. J., Mandin, J. Y., Massie, S. T., Mikhailenko, S. N., Miller, C. E., Moazzen-Ahmadi, N., Naumenko, O. V., Nikitin, A. V., Orphal, J., Perevalov, V. I., Perrin, A., Predoi-Cross, A., Rinsland, C. P., Rotger, M., Šimečková, M., Smith, M. A., Sung, K., Tashkun, S. A., Tennyson, J., Toth, R. A., Vandaele, A. C., and Vander Auwera, J. *J. Quant. Spectrosc. Ra.* **110**(9-10), 533–572 (2009).

[138] Demtröder, W. *Laser Spectroscopy: Basic Concepts and Instrumentation*. Springer-Verslag, (1981).

[139] Bennett, W. R. *Phys. Rev.* **126**, 580–593 (1962).

[140] Lamb, W. E. *Phys. Rev.* **134**, A1429–A1450 (1964).

[141] Chadwick, H., Hundt, P. M., van Reijzen, M. E., Yoder, B. L., and Beck, R. D. *J. Chem. Phys.* **140**, 034321 (2014).

[142] Juurlink, L. B. F. *Eigenstate-resolved measurements of methane dissociation on Ni(100)*. PhD thesis, Tufts University, (2000).

[143] Miller, R. E. *Rev. Sci. Instrum.* **53**, 1719–1723 (1982).

[144] Ebbing, D. D. and Gammon, S. D. *General Chemistry*. Houghton Mifflin Company, 9 edition, (2009).